INVESTIGATIONS ON FREQUENCY AND ENERGY REFERENCES FOR A SPACE-BORNE INTEGRATED PATH DIFFERENTIAL ABSORPTION LIDAR

Andreas Fix[1], Renaud Matthey[2], Axel Amediek[1], Gerhard Ehret[1], Florian Gruet[2], Christoph Kiemle[1], Volker Klein[3], Gaetano Mileti[2], João Pereira do Carmo[4], Mathieu Quatrevalet[1]

[1]Deutsches Zentrum für Luft- und Raumfahrt (DLR), Institut für Physik der Atmosphäre, Oberpfaffenhofen, German. [2]Laboratoire Temps-Fréquence (LTF), Institut de Physique, Université de Neuchâtel, Neuchâtel, Switzerland. [3]Kayser-Threde GmbH, Munich, Germany. [4]ESA-ESTEC, Noordwijk, The Netherlands.

I. INTRODUCTION

For a prediction of the rate of climate change during the 21st century, there is an urgent need to better understand the global carbon cycle, in particular the processes that control the carbon flows between the various reservoirs, and their interactions with the climate system. Atmospheric carbon dioxide (CO_2) represents the main atmospheric phase of this biogeochemical cycle. Due to human activities, the concentration of this most important of the Earth's greenhouse gases has grown from a pre-industrial average atmospheric mole fraction of about 280 parts per million volume (ppm) to 390.5 ppm in 2011 which is an increase of 40 %. CO_2 contributes to ~63 % to the overall global radiative forcing [1].

A powerful tool to improve our knowledge of processes and rates of greenhouse gas (GHG) exchange between atmosphere and biosphere is inverse modelling [2]. Hereby, estimates of fluxes in a chemical transport model are adjusted to provide an improved fit to observations by minimizing the errors in the estimated emissions. For this purpose more highly accurate observations with high spatial resolution and spatial coverage on a global scale are required. Satellite missions have the potential to provide a denser and better distributed set of observations compared to the current network of sparse surface measurements. Thus, there is a need to develop satellite techniques for greenhouse gas observations to improve our knowledge of sources and sinks. However, a very high relative accuracy is necessary, and such accuracy is difficult to achieve from space [3].

The Integrated Path Differential Absorption Lidar (IPDA) technique using hard target reflection in the near IR has the potential to deliver CO_2 column measurements from space with unprecedented accuracy. IPDA largely eliminates the contribution of atmospheric scattering by particles and clouds which greatly affects the achievable accuracy of passive remote sensing instruments. Moreover, this technique can be applied during daytime or night-time and at all latitudes since it does not depend on solar radiation.

Comprising a nadir-viewing CO_2 lidar instrument as the core element, A-SCOPE (Advanced Space Carbon and Climate Observation of Planet Earth) was investigated by ESA as a prephase-A Earth Explorer Mission [4]. A-SCOPE did not yet advance for later phases of the Earth Explorers core missions due to lacking technology readiness; therefore, technology studies such as the one at hand are continued. NASA is pursuing a similar concept with ASCENDS (Active Sensing of CO_2 Emissions over Nights, Days, and Seasons) [5]. The IPDA technique will also be employed by the German-French climate mission MERLIN (Methane Remote Sensing LIDAR Mission) planned for launch around 2019, but for methane (CH_4) as the target greenhouse gas [6].

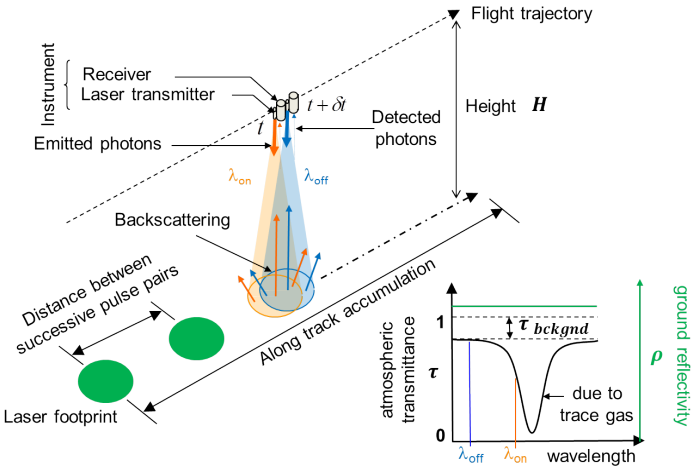

Fig. 1. Principle of the Integrated-Path Differential Absorption (IPDA) lidar technique from satellite.

The necessity to achieve high relative accuracy demands for very stringent system specifications. Within the frame of this investigation the emphasis was put on two paramount requirements: at LTF, a compact frequency reference breadboard was designed to meet the specifications for on-line frequency stabilization. The second requirement, looked after by DLR, relates to the monitoring of on-line to off-line ratio of outgoing pulse energies. Before discussing the experimental results, the requirements of these parameters for an A-SCOPE type IPDA instrument are thoroughly revisited.

II. REQUIREMENTS' DEFINITION

Integrated-Path Differential Absorption (IPDA) lidar uses the laser light scattered back from a surface ("hard target") to obtain measurements of the column content of a specific atmospheric trace gas between lidar and target. Fig. 1 shows the measurement geometry of a nadir-viewing satellite lidar with the measurements aligned along the sub-satellite track. Differential absorption uses the difference in atmospheric transmission between laser emission at a wavelength tuned onto or near the centre of a CO_2 absorption line, denoted on-line, and a reference off-line wavelength with significantly less absorption. Close collocation of the on- and off-line wavelength positions is required to avoid biases by the wavelength-dependency of aerosols, clouds, and the surface. In addition, close spatial beam collocation is mandatory to circumvent biases by the variability of atmospheric and surface scatter.

The quantity of scientific interest is the weighted average of the CO_2 dry-air volume mixing ratio along the probed column, XCO_2, which is given by [8].

$$XCO_2 = \frac{\frac{1}{2}\cdot \ln\left(\frac{P_{off}\cdot E_{on}}{P_{on}\cdot E_{off}}\right)}{\int_{p=0}^{p_{SFC}} WF_{CO_2}(p)\cdot dp} = \frac{DAOD}{IWF} \tag{1}$$

The denominator in (1) is the integral of the so-called weighting function (IWF) along the probed column down to surface pressure (p_{SFC}), determined solely by the temperature and pressure dependent differential absorption cross-section for the considered wavelengths and atmospheric parameters such as air density and humidity that can be obtained from NWP model results. The numerator is the differential atmospheric optical depth, DAOD, where $P_{on/off}$ and $E_{on/off}$ are the measured ground echoes and outgoing pulse energies at the corresponding wavelengths, respectively. Then, assuming Gaussian statistics and no correlation between the different error sources, the total relative systematic uncertainty on the column content XCO_2 is given by differentiating (1):

$$\frac{\delta XCO_2}{XCO_2} = \sqrt{\frac{1}{DAOD^2}\cdot\sum_i\left(\frac{\partial DAOD}{\partial v_i}\cdot\delta v_i\right)^2 + \frac{1}{IWF^2}\cdot\sum_i\left(\frac{\partial IWF}{\partial v_i}\cdot\delta v_i\right)^2} \tag{2}$$

Here, v_i are all variables that are potentially prone to systematic errors and δv_i are the associated systematic error magnitudes. Systematic errors can arise from laser transmitter or receiver errors (e.g. spectral errors induced by unknown laser wavelength instability, laser bandwidth uncertainties, uncertainties in the measurements of the ratio of the on-/offline pulse energies, detector nonlinearity, etc.), atmospheric uncertainties (e.g. temperature, pressure and humidity), from uncertainties in the spectroscopic data base, or from geometric uncertainties (e.g. misalignment between laser and telescope, or unknown Doppler shift due to unidentified mispointing).

In preparation of the A-SCOPE mission, a number of feasibility studies have been undertaken [7][8][9]. The target and threshold mission requirements for the accuracy of the primary data product XCO_2 have been set to 0.05 ppm and 0.15 ppm, respectively, for an observation averaged over 50 km along the satellite track. The allowed target and threshold values for the random error are a factor of ten higher, thus 0.5 ppm and 1.5 ppm, respectively. Using inverse modelling, such error margins would allow for constraining the CO_2 fluxes to within 0.02 Pg/C yr^{-1} on a scale of 1000 x 1000 km^2.

The concepts of "random error" and "systematic error" may be interpreted in terms of uncorrelated and correlated measurement noise, respectively. However, there is an infinite continuum of possible correlations at any timescale in a noisy time series, from fully uncorrelated noise, commonly referred to as white noise, to fully

correlated "noise" such as an unknown linear drift. A powerful mathematical tool to identify and quantify these different types of noises is the Allan variance. A preferred implementation of the latter is the so-called overlapping Allan variance, because it makes use of all the information contained in a given time series y_i of M measurements of a random variable y with even temporal sampling τ_0 [10]:

$$\sigma_y^2(m\cdot\tau_0)=\frac{1}{2\cdot m^2(M-2m+1)}\sum_{j=1}^{M-2m+1}\left\{\sum_{i=j}^{j+m-1}[y_{i+m}-y_i]\right\}^2 \tag{3}$$

where $m\cdot\tau_0$ is the so-called averaging time. The Allan variance (or its square root, the Allan deviation) may be considered to quantify the effect of a gliding average on the magnitude of the noise on y. This is best visualized on a log-sigma versus log-tau plot such as the one of Fig. 2. If the noise is uncorrelated i.e. purely white, its magnitude decreases with averaging time following a -0.5 slope (tau$^{-1/2}$). If correlated noise is present, the decrease may be less steep, and if 1/f noise is present, a "noise floor" will be reached after a certain timescale: further averaging of the data does not reduce the magnitude of the noise because ever stronger low-frequency correlated noise components compensate the reduction of the contribution from higher-frequency noise. For Brown noise with a $1/f^2$ power spectral density, they outweigh it and the magnitude of the noise actually increases with averaging time.

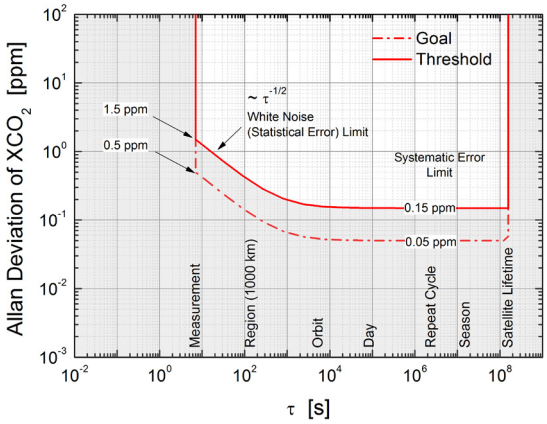

Fig. 2. Template expressing A-SCOPE random and systematic error requirements in terms of Allan deviation.

The above considerations may be applied to the case of A-SCOPE where y is XCO_2. The solid red (respectively, dot-dashed red) curve on Fig.2 has been computed as the geometrical sum of the ideal Allan deviation of pure white noise with a magnitude such that it reaches 1.5 ppm (respectively, 0.5 ppm) at an averaging time of 7 seconds (corresponding to 50 km averaging for a satellite orbiting at 7 km/s), and 1/f noise with a magnitude of 0.15 ppm (respectively, 0.05 ppm). A "continuous" and more rigorous reformulation of the A-SCOPE requirements is for the Allan deviation of the measurement noise to lie under the threshold curve and preferably under the goal curve, i.e in the shaded area of Fig. 2. This reflects the fact that the random error requirement applies to the magnitude of uncorrelated noise at short averaging times, while the systematic error requirement puts an upper limit to the magnitude of correlated errors at "long" timescales up to the satellite lifetime.

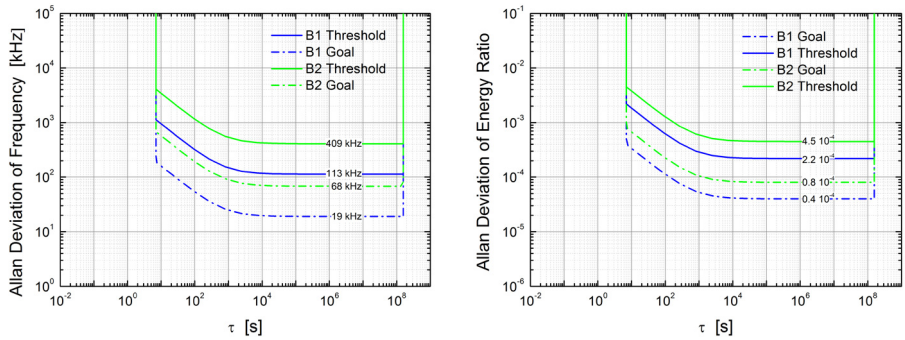

Fig. 3. Templates for the acceptable error for on-line frequency stability (left) and energy ratio (right). The curves are given for threshold and goal requirements as well as for the two possible wavelength pairs.

From this template, the requirements for the on-line frequency stabilization as well as for the energy ratio (E_{on}/E_{off}) were derived using (2) under the assumption that for the threshold (goal) case the individual contribution must not exceed 50% (25%) of the total error budget. Since for CO_2 IPDA two possible wavelength sets at 1.57µm (B1) and 2.05 µm (B2) have been identified as suitable for measurement from space, this calculation was performed for both wavelength options. The corresponding results are depicted in Fig. 3. Due to its more favourable weighting function the requirements are not as stringent for the 2.05-µm spectral range. These requirements serve as the benchmark for the following breadboard studies for which the spectral region at 1.57 µm has been chosen, since here the requirements are more stringent but also optical components in this wavelength range are more readily available.

III. FREQUENCY REFERENCE BREADBOARD

To reach the target frequency stability and accuracy, a frequency reference laser system was built around a single-mode laser stabilized onto a rubidium (Rb) cell and an optical frequency comb (OFC) employed to fill the gap between the frequency reference and the lidar laser transmitter wavelength. The laser system is schematically depicted in Fig. 4.

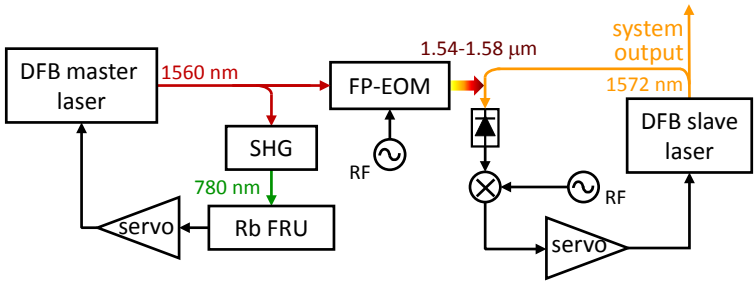

Fig. 4. Diagram of the laser system. FP-EOM: Fabry-Perot electro-optical modulator; SHG: second harmonic generation; Rb FRU: Rubidium frequency reference unit; RF: radio-frequency oscillator.

Rubidium has been preferred to CO_2 as an absolute frequency reference, as it exhibits strong and narrow sub-Doppler transition lines (20-30 MHz, FWHM) at 780 nm achievable with low laser power (below 0.5 mW). A custom home-mode centimetre-scale Rb-filled glass cell is sufficient to frequency lock a laser whereas an optical path length of several meters or more is needed for Doppler-broadened CO_2 lines (~400 MHz, FWHM) [11].

A fibre-pigtailed DFB laser emitting at 1560 nm serves as master laser source. For frequency stabilisation, part of its output is frequency doubled using a fibre-coupled converter unit built around a PPLN waveguide. The 780-nm light ends up in a compact reference unit (Rb FRU) [12], where it probes Rb atoms in a saturated absorption scheme. Frequency locking to the Rb transition is achieved by wavelength modulation spectroscopy and feedback to the laser diode current. The measured saturated absorption spectrum is depicted in Fig. 5.

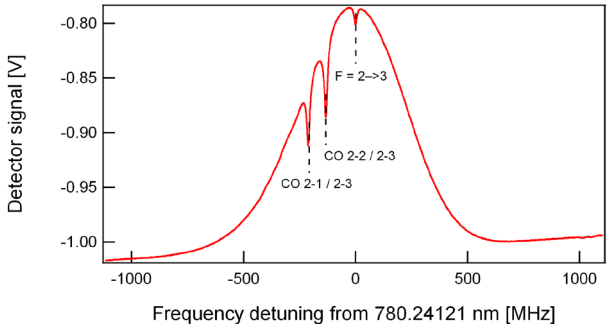

Fig. 5. Rubidium D2 absorption lines at 780 nm (Fg=2 hyperfine ground state) recorded with the cell assembly. Narrow sub-Doppler features are clearly visible.

To transfer the stability into the vicinity of the CO_2 absorption line at 1572 nm, an OFC bridges the 12-nm gap from the doubled Rb wavelength at 1560 nm. It is realized by modulating at 10 GHz the remaining part of the master laser light with a waveguide electro-optical modulator enclosed in a Fabry-Pérot cavity (see Fig.4) [13]. The obtained OFC consists of equidistant lines separated by 10 GHz (~80 pm) from each other and exhibits a span of more than 45 nm, as illustrated in Fig. 6, spreading over the target CO_2 line region.

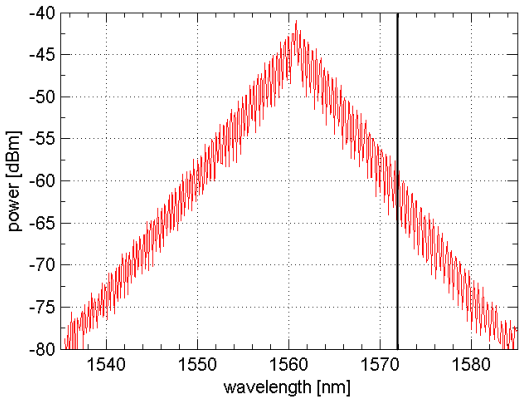

Fig. 6. Span of the OFC obtained when injecting the FP-EOM with 26 dBm of RF power, at 10-GHz modulation frequency. The solid line indicates the target CO_2 absorption line at 1572.0 nm.

In order to demonstrate the frequency stability of the laser system, the wavelengths at 780 nm and 1560 nm were first monitored simultaneously using beat-note measurements. At 780 nm the output of the SHG was heterodyned with a second Rb-stabilized reference laser with a known (relative) frequency stability of better than $1 \cdot 10^{-11}$ at all timescales between 1 s and one day. At 1560 nm, the output of the master laser was heterodyned with a commercial self-referenced Er-fibre frequency comb. To ensure its long-term frequency stability, this self-referenced comb is stabilized onto a hydrogen maser (through its frequency carrier envelop offset and repetition rate). Since the maser exhibits a relative frequency stability of better than $4 \cdot 10^{-14}$ for $\tau > 10$ s, this enables to measure absolute optical frequencies to within < 50 Hz.

Long-term measurements have been performed with the master laser locked onto either the crossover CO21-23 or the direct F=2→3 transition (see Fig. 5). Due to its lower temperature sensitivity the latter one results in a slightly improved long-term stability. The result of a 12-day measurement exhibits a perfect match between both measurements at 780 nm and 1560 nm, as depicted in Fig. 7. A beat-note fractional stability of better than $1 \cdot 10^{-11}$ was reached for time scales of > 1000 s. This outperforms the project goal requirements (19 kHz at 1572 nm, equivalent to a fractional value of $1 \cdot 10^{-10}$) by a factor of ten.

Within another sequence of beat-note experiments it could be shown that the stability of the OFC teeth are not visibly degraded and thus remains equivalent to the one of the master laser. In Fig. 6 is also reported the stability of a line of the OFC situated at 1557 nm, obtained by heterodyning the OFC with a 1557-nm DFB laser that was stabilized to the self-referenced Er-fibre frequency comb. The OFC stability at 1557 nm faithfully reproduces that of the master laser. Offset-locking a slave reference or seed laser to an appropriate line of the OFC is thus expected to provide a sufficiently stable laser source at the CO_2 wavelength.

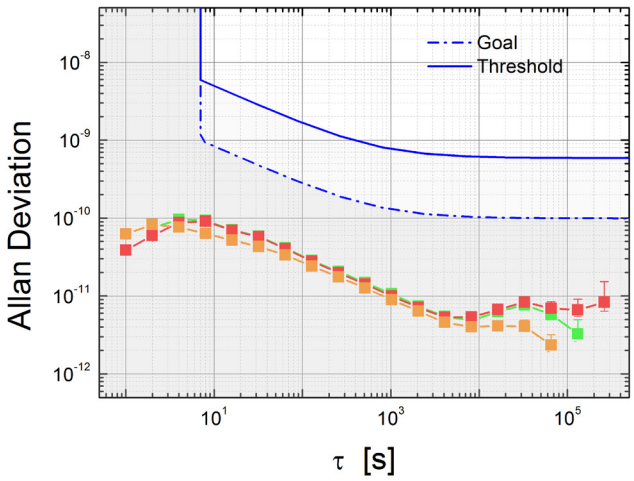

Fig. 7. Long-term relative beat-note frequency stability expressed in terms of Allan deviation for different components of the stabilized laser system: at 780 nm (green), at 1560 nm (red), and at 1557 nm (orange). See text for details. A relative value of $1 \cdot 10^{-11}$ corresponds to ~2 kHz at 1560 nm.

IV. ENERGY RATIO MONITORING INVESTIGATIONS

The second requirement relates to the monitoring of the on-line to off-line ratio of outgoing pulse energies, whereby accuracy of the order of 10^{-4} is pursued (Fig. 3). The preferred set-up would use an identical detector for both lidar signal and pulse energy monitor to circumvent potential detector ageing effects. It is thus important to employ pick-up, attenuation, transmit and detection schemes that do not alter the energy ratio. For this purpose, the use of integrating spheres has been suggested in [4], since those are insensitive to beam pointing and intensity profile variations and can be fibre-coupled. However, given the coherence of the lidar transmitter, speckle effects need to be considered in detail. Therefore, a pulsed laser test bed was used to investigate possible monitoring schemes (Fig. 8) based on an optical parametric oscillator (OPO).

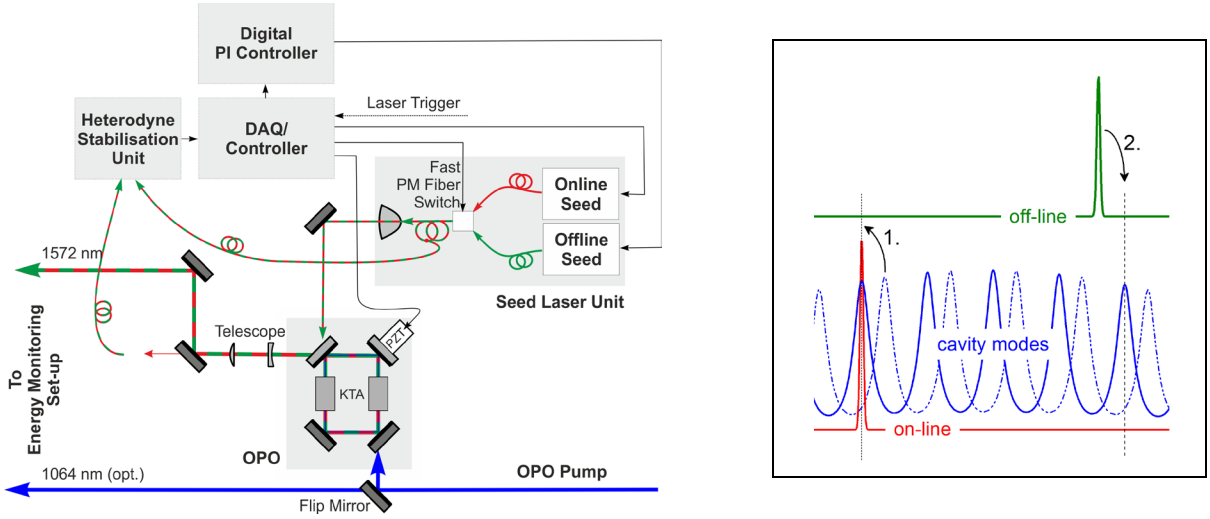

Fig. 8. Set-up of the optical parametric oscillator (left) and schematic of the method to stabilise the OPO cavity to the on-line laser and the off-line to the OPO (right).

The OPO uses KTA as the non-linear optical material and is pumped by an injection-seeded, diode pumped Nd:YAG laser [14]. The laser can be operated in double pulse mode thereby emitting two pulses with a separation of ~360 µs at a 50-Hz rate, or at 100 Hz single pulse. Narrowband operation of the OPO is achieved by injection seeding using two DFB fibre lasers. By means of a fast fibre switch the seed wavelength can be altered from pulse to pulse. The OPO is matched to the seed using a heterodyne stabilisation technique [14]. Since an independent control for on-line and off-line stabilisation would result in high dynamic load on the PZT element, an alternative control was used (Fig. 8) for double pulse operation: the OPO cavity is matched to the on-line seed wavelength, whereas the off-line laser is tuned onto a nearby cavity mode of the OPO using a digital feedback loop controlling the piezo of the DFB fibre laser. In some of the cases described below, the Nd:YAG laser radiation was used within the energy monitoring experiments. For this purpose, a flip mirror transmitted the beam to the experiment.

One of the main challenges when determining the accuracy of the energy ratio measurement is the lack of a reference system that may serve to provide the “true” value against which the experimental set-up can be referenced. Therefore the energy ratios had to be simultaneously measured twice using the same or different measurement technique and analysed using statistical methods. Again, the Allan variance is used to identify uncorrelated and correlated measurement noise. Since thermal detectors are generally to slow to resolve individual pulses, only detectors based on the pyroelectric or photoelectric effect are to be considered.

In a series of experiments (using the Nd:YAG laser only) it was shown that the pyroelectric detectors used were rather insensitive to temperature variations. Moreover, they exhibit a high linearity over > 4 orders of magnitude. However, differences in beam steering of on-line and off-line pulse onto the sensitive area may limit the accuracy. Therefore integrating spheres are attractive since they are insensitive to beam variations. This was verified by modulating the angle of the beam impinging onto a sphere.

Integrating spheres also provide an adequate means for wavelength-independent attenuation. Using established theory [15], the attenuation can be accurately predicted also for double integrating sphere arrangement with diffusor sheets in between.

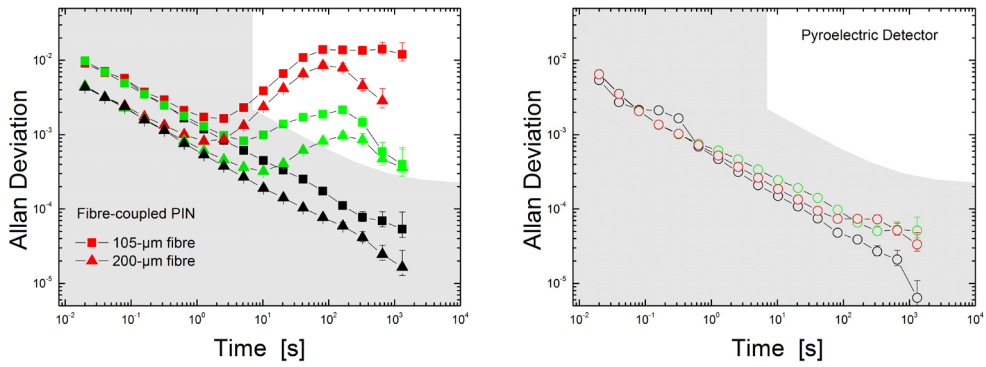

Fig. 9. Allan deviations of the pulse energy ratio of two subsequent pulses divided by the same ratio recorded with a second detector. The nominal on-line/off-line double pulse sequence is given in red. Green symbols designate the double pulse mode but no switching of wavelengths whereas the result for a single pulse (100Hz) sequence is given in black. The left panel shows the results for PIN diodes fibre-coupled to the integrating spheres for two pick-up fibre diameters of 105 µm and 200 µm, respectively, and the right display for pyroelectric detectors. In order to meet the threshold requirements, the curves have to remain in the shaded area.

However, it is well known that integrating spheres generate speckle from narrowband laser sources [16] that may give rise to additional noise of the energy ratio. The speckle patterns at the exit port of integrating spheres of two subsequent pulses within a double-pulse sequence of ~ 360 µs appear to be partly correlated. This is depicted in Fig. 9. While the Allan deviation of the energy ratio of single pulses with a separation time of 10 ms results in an almost ideal -0.5 slope, this is not true for the double pulse mode. Since the noise is reduced with the number of speckle captured, the effect is most prominent for a small (105-µm) fibre. But even for the large pyroelectric detector having a sensitive area of 10 mm some deviations are seen at the $\sim 5 \cdot 10^{-5}$ level (Fig. 9). This value, albeit already within specifications (see Fig.3), is in agreement with the number of objective speckles seen by this detector. In order to destroy this correlation, several methods have been evaluated. Vibrating the spheres by coupling them to a sonic transducer led to marginal improvement, though better results were achieved by means of reducing the speckles by angular diversity, i.e. the bare fibre ends were mechanically vibrated (Fig. 10). By temperature cycling of the sphere the peak seen at ~100s could be shifted in time.

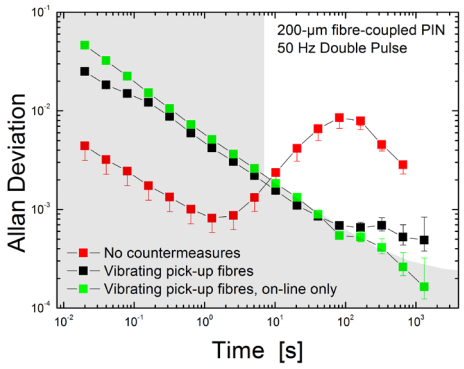

Fig. 10. Allan deviations of the pulse energy ratio of two subsequent pulses divided by the same ratio recorded with a second detector. Shown are three cases: without countermeasures against the speckle correlation, and employing vibrating pick-up fibres for the nominal on-/offline sequence and for on-line only, respectively.

As a conclusion, speckle effects are to be considered for measuring the energy ratio of the outgoing pulses of an IPDA laser transmitter. Due to their large sensitive area, pyroelectric detectors are less prone to this noise, but their employment would require deviating from the concept of measuring the return pulses and outgoing pulse energy with the same detector. For photoelectric detectors which are fibre coupled to integrating spheres the speckle correlation needs to be reduced to meet the requirements. With the described means, the threshold requirements were already almost met. Further investigations are in progress.

V. SUMMARY

The IPDA technique shows much promise for greenhouse gas monitoring from space but demands for very stringent system requirements. Those have carefully been revised and a benchmark using the Allan variance has been introduced which was applied to two distinct requirements. The required frequency stability in the 1.57-µm region was experimentally outperformed by locking the second harmonic of a 1560-nm laser to a Doppler-free rubidium line. The gap between 1560 nm and the region of the CO_2 absorption lines at 1572 nm is bridged by means of an optical frequency comb. It was shown that high frequency stability could be transferred from the Rb reference to the CO_2 absorption region. Due to its coherence, the measurement of the energy ratio of the laser pulses is hampered by speckle effects. By using pyroelectric energy detectors at the exit ports of integrating spheres the relative systematic error of the energy ratio measurement of double pulse pairs could be reduced to stay within the goal requirements ($\sim 5 \cdot 10^{-5}$) over time scales of a few hours. When using fibre-coupled detectors, remedies have been analysed that either use angular diversity or sweep the temperature of the sphere.

ACKNOWLEDGMENTS

We would like to thank M. Wirth and H.R. Khalesifard for experimentally supporting the energy monitoring experiments and S. Schilt for his assistance in the frequency stability measurements with the self-referenced comb. This work is supported by the European Space Agency and the Swiss National Research Foundation.

REFERENCES

[1] P. Ciais, et al., 2013: Carbon and Other Biogeochemical Cycles. In: *Climate Change 2013: The Physical Science Basis. Contribution of Working Group I to the Fifth Assessment Report of the Intergovernmental Panel on Climate Change*, Cambridge University Press, Cambridge, UK and New York, NY, USA.

[2] K.R. Gurney, et al. "Towards robust regional estimates of CO2 sources and sinks using atmospheric transport models," *Nature* 415, pp. 626-630, 2002.

[3] F.-M. Bréon, P. Ciais, "Spaceborne remote sensing of greenhouse gas concentrations," *C. R. Geoscience* 342, pp. 412–424, 2010.

[4] ESA, *A-SCOPE - Advanced space carbon and climate observation of planet earth*, Report for Assessment, SP-1313/1, ESA-ESTEC, Noordwijk, The Netherlands, ISBN 978-92-9221-406-7, 2008.

[5] National Research Council. *Earth Science and Applications from Space: A Midterm Assessment of NASA's Implementation of the Decadal Survey*, Washington, DC: The National Academies Press, 2012.

[6] C. Stephan, M. Alpers, B. Millet, G. Ehret, and P. Flamant, "Methane Monitoring from Space," *Proc. International Conference on Space Optics (ICSO),* 2012.

[7] G. Ehret, C. Kiemle, M. Wirth, A. Amediek, A. Fix, and S. Houweling, "Space-borne remote sensing of CO2, CH4, and N2O by integrated path differential absorption lidar: a sensitivity analysis," *Appl.Phys. B* 90, pp.593-608, 2008.

[8] R.T. Menzies and D.M. Tratt, "Differential laser absorption spectrometry for global profiling of tropospheric carbon dioxide: selection of optimum sounding frequencies for high-precision measurements," *Appl. Opt.* 42, pp. 6569–6577, 2003.

[9] J. Caron, and Y. Durand, "Operating wavelengths optimization for a spaceborne lidar measuring atmospheric CO2," *Appl. Opt.* 48, pp. 5413-5422, 2009.

[10] W.J. Riley, *Handbook of Frequency Stability Analysis*, NIST Special Publication 1065, National Institute of Standards and Technology, Boulder, CO, 2008.

[11] K. Numata., J.R. Chen, S.T. Wu, J.B. Abshire, M.A. Krainak., "Frequency stabilization of distributed-feedback laser diodes at 1572 nm for lidar measurements of atmospheric carbon dioxide," *Appl. Opt*. 50, pp. 1047-1056, 2011.

[12] F. Gruet, M. Pellaton, C. Affolderbach, T. Bandi, R. Matthey, and G. Mileti, "Compact and frequency stabilized laser heads for Rubidium atomic clocks", *Proc. International Conference on Space Optics (ICSO),* 2012.

[13] M. Kourogi, K. Nakagawa, M. Ohtsu,"Wide-span optical frequency comb generator for accurate optical frequency difference measurement," *IEEE Journal of Quantum Electronics*. 29, pp. 2693-2701, 1993.

[14] A. Fix, C. Büdenbender, M. Wirth, M. Quatrevalet, A. Amediek, C. Kiemle, and G. Ehret, "Optical parametric oscillators and amplifiers for airborne and spaceborne active remote sensing of CO2 and CH4," *Proc. SPIE* 8182, pp. 818206, 2011.

[15] J.W. Pickering, S.A. Prahl, N. van Wieringen, J.F. Beek, H.J.C.M. Sterenborg, and M.J.C. van Gemert, "Double-integrating-sphere system for measuring the optical properties of tissue," *Appl. Opt.* 32, pp. 399-410, 1993.

[16] G.D. Boreman, A.B. Centore and Y. Sun, "Generation of laser speckle with an integrating sphere," *Opt. Eng.* 29, pp. 339-342, 1990.